



# An experimental approach for estimating the impedance of elastic non-porous materials

Matthieu Hartenstein<sup>1</sup>, Efren Fernandez-Grande<sup>2,\*</sup>, Vicente Cutanda-Henriquez<sup>2,\*</sup>

<sup>1</sup>DTU Electrical Engineering, Technical University of Denmark, Lyngby 2800, Denmark

<sup>2</sup>DTU Electrical Engineering, Technical University of Denmark, Lyngby 2800, Denmark

\*{efg@elektro.dtu.dk}

## Abstract

Human skin is generally assumed to be acoustically rigid. It has been shown that it almost totally reflects sound waves, without significant dissipation of energy. Yet, it appears that the propagation of sound around the human body is influenced by the acoustic properties of skin tissue (this is for example observed in the simulation of head-related transfer functions or in ear-canal reflectance measurements). In general, estimating the impedance of highly reflective materials is experimentally challenging. In this work, the feasibility of the impedance estimation of nearly acoustically rigid bodies via the equivalent source method is assessed. A semi-analytical solution to the problem of scattering of sound by an elastic body with a rigid core is derived. The solution of this problem is used as a validation benchmark for the proposed impedance estimation method. Experimental tests with real data are also presented and compared against the model result.

**Keywords:** human skin, impedance estimation, ESM, scattering.

## 1 Introduction

Scattering of sound by the human head and torso leads to time and amplitude sound pressure differences between the left ear and the right ear. These inter-aural differences are fundamental in the human sound localization process [1]. Thus, a broad range of applications, including the testing of hearing assistive devices [2] and the development of virtual audio methods [3], demands a precise knowledge of the sound field close to the human head. When simulating numerically the sound field scattered around an object, via e.g. the boundary element method, knowledge of the surface impedance of the object is needed in order to model boundary conditions [4]. In acoustic simulations of the sound field around a head, including the estimation of Head Related Transfer Functions (HRTF), human skin is generally assumed to be rigid. Yet, it has been shown that using different materials for crafting the pinnae of an acoustic measurement dummy head leads to changes in the measured HRTF [5]. These changes are particularly significant at mid to high frequencies, at which the complex details of the head, and particularly of the pinna, induce a substantial amount of reflexions. The knowledge of the impedance of human skin could thus help improving HRTF simulations, allowing to relax the rigid scattering hypothesis.

In this work, the feasibility of estimating the normal impedance of human skin with near-field acoustic holography (NAH) is assessed. A source emits sound towards a human arm, and a double-layer array of microphones is placed close to the surface of the arm. NAH has already been used to measure acoustic impedances and reflection coefficients of porous materials, and was shown to give accurate estimates [6, 7, 8].

The equivalent source method (ESM) is used to recover the incident and scattered fields on the surface of a scattering object as a superposition of fields coming from equivalent sources placed respectively inside and outside of the object [9, 10, 11]. Despite the number of parameters (number of equivalent sources to use [12], retreat distance between the inner sources and the scattering object's surface [13]) that have to be chosen, this method is fairly simple to implement and has been shown to give accurate results [12, 14]. It also presents the

advantage to be adaptable to different surface geometries. Moreover, the equivalent source method is one of the NAH methods that has already been shown to be an efficient tool to estimate the impedance of absorptive surfaces [6, 8].

The impedance estimation framework is tested numerically on a model of sound scattering by a human arm. The model is based on the analytical solution to the problem of scattering of sound by an elastic cylinder with a rigid core, derived in this work. A first attempt to estimating the impedance of human skin is also presented.

## 2 Scattering of sound by an elastic cylinder

The vibro-acoustic problem of scattering of a plane wave by an elastic cylinder is solved in this section. The cylinder has a rigid core in order to model the configuration of a human arm. It is supposed to be infinite in the axial direction, which allows to work in a polar coordinate system  $(r, \theta)$ . The solution to this problem will be used later to test the impedance estimation method.

All the acoustic and elastic fields in this section and in the rest of this paper will be assumed to follow a time-harmonic dependency  $e^{j\omega t}$ , that will be omitted.

### 2.1. Acoustic fields

The total acoustic field  $p$  around the cylinder can be decomposed as  $p = p_i + p_s$ , where  $p_i$  is the incident field that would exist without the cylinder, and  $p_s$  is the so-called scattered field.

Both  $p$  and  $p_i$  satisfy the Helmholtz equation  $\Delta p + k^2 p = 0$ , where  $k = \frac{\omega}{c_0}$  is the acoustic wavenumber.

The incident plane wave  $p_i = e^{-jkx}$  of unitary amplitude can be expanded in a cylindrical wave basis [15] ( $J_n$  is a Bessel function of first kind and order  $n \geq 0$ )

$$p_i(r, \theta) = \sum_{n=0}^{+\infty} (-j)^n \epsilon_n J_n(kr) \cos(n\theta), \quad (1)$$

with  $\epsilon_n = 1$  for  $n = 0$  and  $\epsilon_n = 2$  for  $n > 0$ .

As a linear combination of  $p$  and  $p_i$ ,  $p_s$  also satisfies the Helmholtz equation. Under the assumption that it satisfies Sommerfeld's radiation condition, it can be expressed as a sum of waves outgoing from the cylinder [16] (in this work,  $H_n^{(i)}$  denotes the Hankel function of the  $i$ -th kind and order  $n$ ,  $i \in \{1, 2\}$  and  $n \geq 0$ )

$$p_s(r, \theta) = \sum_{n=0}^{+\infty} \alpha_n H_n^{(2)}(kr) \cos(n\theta). \quad (2)$$

Note that the symmetry of the problem about  $\theta = 0$  allows to restrict the  $\theta$  dependency to a cosine expansion. This symmetry argument will be used again when deriving the elastic fields.

The normal incident and scattered velocities  $u_i$  and  $u_s$  can be derived from Equation 1 and 2 making use of Euler's equation of motion.

### 2.2. Mechanical fields

In what follows, the density of the elastic medium will be denoted  $\rho_M$ . Its Lamé coefficients will be denoted  $\lambda$  and  $\mu$  and can be retrieved from the Young's modulus and Poisson's ratio of the elastic material of interest.

The fundamental equations involving the 2x2 stress matrix  $\sigma$  and the 2x1 displacement vector  $\xi$  in the elastic model are the mechanical equilibrium equation and Hooke's law.

The elastic displacement can be decomposed as [16]:

$$\xi = -\mathit{grad}(\psi) + \mathit{rot}(\phi), \quad (3)$$

where the scalar  $\psi$  and the vector  $\phi$  are respectively the compression and shear potentials. Note that in a 2D cylindrical problem, the shear potential is reduced to its axial component, that will be denoted  $\phi$ . The potentials can be solved for independently as superpositions of cylindrical waves, making use of the symmetries of the problem:

$$\psi(r, \theta) = \sum_{n=0}^{+\infty} \cos(n\theta)(A_n H_n^{(1)}(k_p r) + B_n H_n^{(2)}(k_p r)), \quad (4)$$

$$\phi(r, \theta) = \sum_{n=0}^{+\infty} \sin(n\theta)(C_n H_n^{(1)}(k_s r) + D_n H_n^{(2)}(k_s r)), \quad (5)$$

where  $k_p = \frac{\omega}{c_p}$  and  $k_s = \frac{\omega}{c_s}$  are respectively the compression and shear wavenumbers. The compression and

shear wave speeds are respectively given by  $c_p = \sqrt{\frac{\lambda + 2\mu}{\rho_M}}$  and  $c_s = \sqrt{\frac{\mu}{\rho_M}}$ .

The elastic displacement can be retrieved making use of Equation 3. The components of the stress matrix which are needed to solve the coupled acoustic-mechanical problem are the radial and tangential components of the direct stress, respectively  $\sigma_{rr}$  and  $\sigma_{r\theta}$ . They can be derived from the radial and tangential displacements  $\xi_r$  and  $\xi_\theta$  via Hooke's law.

### 2.3. Boundary conditions

Five boundary conditions are needed in order to close the coupled acoustic-elastic problem.

All around the cylinder, the radial component of the direct elastic stress and the acoustic pressure satisfy an equilibrium. The tangential component of the direct elastic stress is null (there is no acoustic shear force at the surface of the cylinder). Eventually, the radial velocity at the surface of the cylinder must follow the radial acoustic particle velocity. These boundary conditions are expressed in respectively Equations 6, 7 and 8.

$$\sigma_{rr}(r_2, \theta) + p_s(r_2, \theta) = -p_i(r_2, \theta). \quad (6)$$

$$\sigma_{r\theta}(r_2, \theta) = 0. \quad (7)$$

$$j\omega\xi_r(r_2, \theta) - u_s(r_2, \theta) = u_i(r_2, \theta). \quad (8)$$

At the boundary between the core of the cylinder and the elastic medium, the radial and tangential components of the elastic displacement vanish:

$$\xi_r(r_2, \theta) = 0. \quad (9)$$

$$\xi_\theta(r_2, \theta) = 0. \quad (10)$$

Using the orthogonality of the cosine functions in the cylindrical expansion, Equations 6 to 10 can be written for each term  $n$  of the expansion as a linear system of equations in terms of the coefficients  $\alpha_n$ ,  $A_n$ ,  $B_n$ ,  $C_n$  and  $D_n$ .

## 3 Impedance estimation method

In this work, a human arm is illuminated with a sound source. The equivalent source method (ESM) is used to infer the acoustic fields at the surface of the arm from near-field measurements.

The ESM lies on the assumption that the sound field of interest can be reconstructed as a sum of contributions coming from a distribution of point sources [9]. The incoming incident field is assumed to come from point sources located on a surface outside the scattering object, while the point sources used to construct the outgoing scattered field are located inside the object [11]. An example of ESM setup is shown Figure 3.

The acoustic pressure  $p$  can then be written as a sum of contribution from  $N$  points sources  $i$  located at the position  $r_i$  with volume velocity  $Q_i$ :

$$p(\mathbf{r}) = \sum_{i=1}^N Q_i G(\mathbf{r}, \mathbf{r}_i), \quad (11)$$

where  $G$  is the Green's function in free-field. In this work, the problems are two-dimensional and  $G(\mathbf{r}, \mathbf{r}_0) = \frac{j}{4} H_0^{(1)}(k|\mathbf{r} - \mathbf{r}_0|)$ .

The particle velocity in the direction  $\mathbf{n}$  can be derived from Equation 11 via Euler's equation of motion :

$$u(\mathbf{r}) = j\omega \sum_{i=1}^N Q_i \frac{\partial G}{\partial \mathbf{n}}(\mathbf{r}, \mathbf{r}_i), \quad (12)$$

where  $\frac{\partial G}{\partial \mathbf{n}}$  denotes the derivative of  $G$  in the direction  $\mathbf{n}$ .

### 3.1. Analysis

Assuming that the pressure field is captured at  $M$  measurement points on a surface  $h$  close to the scattering surface, the known vector of measurements  $\mathbf{P}_h$  (size  $M$ ) can be linked to the vector of source strengths  $\mathbf{Q} = [Q_i]$  via a matrix of Green's function values  $\mathbf{G}_{ES-h} = [G(\mathbf{r}_m, \mathbf{r}_i)]$  linking the  $N$  point source locations  $\mathbf{r}_i$  to the  $M$  measurement points  $\mathbf{r}_m$ :

$$\mathbf{P}_h = \mathbf{G}_{ES-h} \mathbf{Q}. \quad (13)$$

The source strengths can be recovered via a standard L2-regularized inversion ([11]). The optimal regularization parameter is found by means of generalized cross-validation ([17]).

### 3.2. Synthesis

The vectors of pressure  $\mathbf{P}_S$  and normal velocities  $\mathbf{U}_S$  on  $K$  points  $k$  at positions  $\mathbf{r}_k$  of the scattering surface  $S$  can be reconstructed from the source strengths making use of Equation 11 and Equation 12:

$$\mathbf{P}_S = \mathbf{G}_{ES-S} \mathbf{Q}, \quad (14)$$

$$\mathbf{U}_S = \mathbf{H}_{ES-S} \mathbf{Q}, \quad (15)$$

where  $\mathbf{G}_{ES-S} = [G(\mathbf{r}_k, \mathbf{r}_i)]$  and  $\mathbf{H}_{ES-S} = [\frac{\partial G}{\partial \mathbf{n}_k}(\mathbf{r}_k, \mathbf{r}_i)]$ ,  $\mathbf{n}_k$  being the normal to the scattering surface at  $\mathbf{r}_k$ .

Eventually, an impedance map can be reconstructed on the surface of the object as the ratio of the reconstructed pressure to the reconstructed velocity. The impedance of the object can be estimated locally as a spatial average.

## 4 Numerical results

### 4.1. Sound scattering model

The model of sound scattering by an elastic cylinder is numerically built-up on the frequency range [1,20] kHz. This geometry emulates the shape of a human arm. The cylindrical expansions of the field are truncated to a sufficient amount of terms  $N_{trunc}$  such as  $N_{trunc} \approx \max(k_p r_2, k_s r_2, k r_{ac})$ , where  $r_{ac}$  is the radius of the acoustic domain of consideration. This truncation condition should allow consistent reconstruction of both the elastic waves in the cylinder and the acoustic waves in the fluid.

The coefficients of the acoustic and elastic fields' cylindrical expansions are retrieved by numerical inversion of the system of boundary equations introduced section 2. The mechanical properties used to describe the elastic cylinders are typical of silicone (density  $\rho = 1500 \text{ kg.m}^{-3}$ , Young's modulus  $E = 30 \text{ MPa}$ , Poisson ratio  $\nu = 0.47$ , loss factor  $\eta = 0.2$ , taken from [18] and [19]). The internal (resp. external) radius of the elastic domain in the cylinder are  $r_1 = 2.5 \text{ cm}$  (resp.  $r_2 = 3 \text{ cm}$ ).

The obtained pressure field is shown Figure 1 at two frequencies, around 1 and 15 kHz. At both frequencies, the solutions are close to the ones obtained with an acoustically rigid cylinder. Around 1 kHz (left figure), the main scattering effect is a rise in pressure in front of the cylinder. Around 15 kHz, where the radius of the cylinder is twice higher than the acoustic wavelength, a scattering effect similar to the one of a rigid cylinder is observed. An interference pattern occurs in front of the cylinder, with a rise in pressure amplitude of about twice the incident pressure amplitude at the surface of the cylinder. The pressure amplitude towards the back of the cylinder is lower than 0.5 the incident pressure amplitude, due to the shadow of the cylinder.

The impedance of the elastic cylinder at normal incidence is shown Figure 2. The reactive part of the impedance is one order of magnitude higher than its resistive part, and the reactance is positive. Its amplitude decreases inversely proportionnal to the frequency below 2 kHz. These properties are characteristic of a compliant behaviour. At these frequencies, only compression waves exist in the coating. The front of the cylinder compresses and expands in response to the incident wave. At higher frequencies, the reactance amplitude decrease with frequency is steeper, which could be due to shear waves appearing in the coating. Around 17 kHz, a notch appears on the reactance amplitude. At this frequency, the product  $k_p h$  ( $h$  being the coating's thickness) is about  $\frac{\pi}{2}$  and a mechanical resonance appears. Indeed, a compression wave propagating in the  $x$  direction and reflecting on the cylinder's core would arrive back at the surface of the coating with a phase delay of  $\pi$ . Note that the resistive part of the impedance is non-zero, which is due to structural losses included in the vibro-acoustic model via a complex Young's modulus. Note that the absolute value of the cylinder's impedance presents very high values compared to the characteristic impedance of air (up to about  $10^4 \rho_0 c_0$ ).

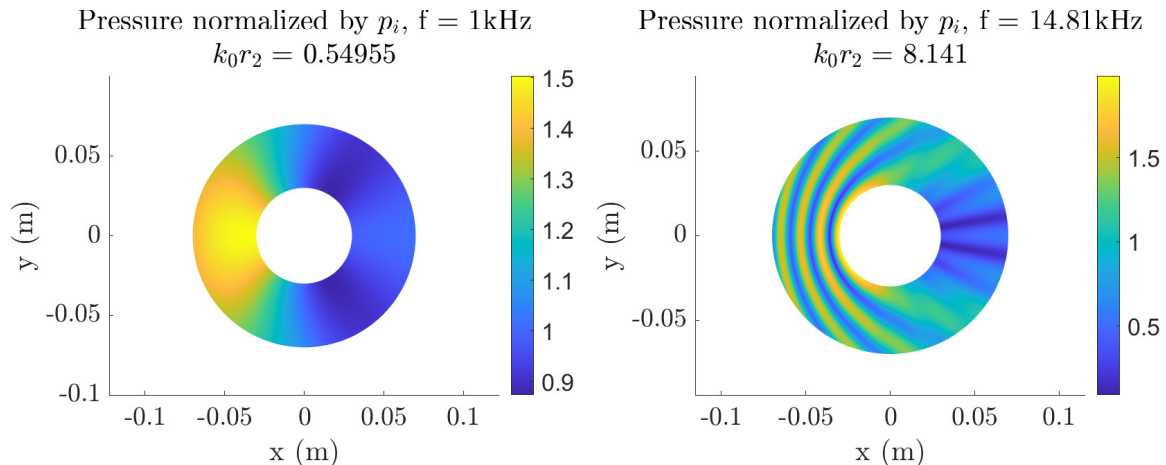


Figure 1: Pressure amplitude of a plane wave scattered by an elastic cylinder. The total pressure  $p$  is normalized by the incident pressure  $p_i$ . Left: Low frequency where  $k_0 r_2 < 1$ . Right : High frequency where  $k_0 r_2 > 10$ .

#### 4.2. ESM setup

The proposed impedance estimation method is tested on the benchmark case of scattering by an elastic cylinder of silicone with a rigid core developed section 2. The pressure measurements are numerically computed using the same parameters as in subsection 4.1. As explained in section 3, two layers of microphones and equivalent sources are needed in order to reconstruct the incident and scattered fields. The ESM setup is shown Figure 3.

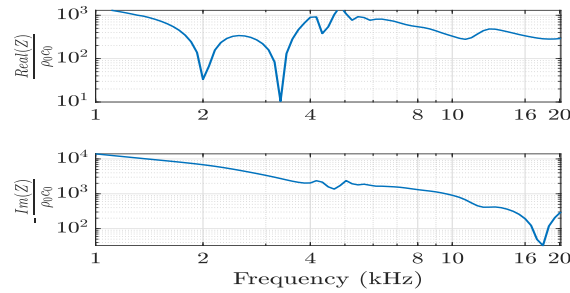


Figure 2: Real and imaginary parts of the impedance of the elastic cylinder at normal incidence.

A gaussian additive noise is added to the pressure measurement in order to perform the reconstruction in two configurations. In the first configuration, the signal to noise ratio (SNR) is virtually infinite and the ESM reconstruction is based on measurements on a single realization. This configuration is regarded as "noiseless". In the second configuration, the signal to noise ratio is fixed to 30 dB, and the measurements are averaged on 50 realizations. This configuration will be later referred to as "noisy". After the ESM reconstruction, the normal impedance of the coating is estimated as an impedance average on a cone of 10 degrees around normal incidence.

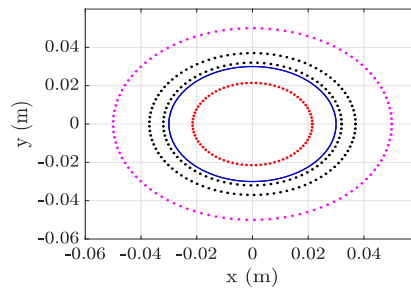


Figure 3: Setup used for the numerical tests of the ESM reconstruction. Blue circle: reconstruction surface, red dots: inner equivalent sources, magenta dots: outer equivalent sources, black dots: measurement points. The measurement surfaces are respectively located 2 and 7 mm from the reconstruction surface, and sampled with respectively 84 and 98 points. There are 80 inner equivalent sources located 8.5mm from the surface, and 114 outer equivalent sources located 20 mm from the surface.

### 4.3. Results of the ESM reconstruction

The pressure reconstruction at 3 kHz is shown on the top part of Figure 4, in the "noiseless" and "noisy" cases. In both cases, the pressure reconstruction is accurate all over the cylinder.

The figure at the bottom of Figure 4 shows the velocity reconstructed on the surface of the cylinder in a case where the pressure measurements are not contaminated by noise, and in a case where they are. The red dashed curve (noiseless case) follows the true velocity (continuous blue curve), which shows that the velocity reconstruction works well in absence of noise. However, in presence of noise (yellow dashed curve), high spatial frequency components appear in the velocity reconstruction. In terms of amplitude, these components are comparable to the true solution. These high spatial frequency components are due to measurement noise that is amplified in the pressure to velocity reconstruction. The noise amplification issue is emphasized by the normal velocity amplitude at the surface of the cylinder, due to the high impedance of the coating.

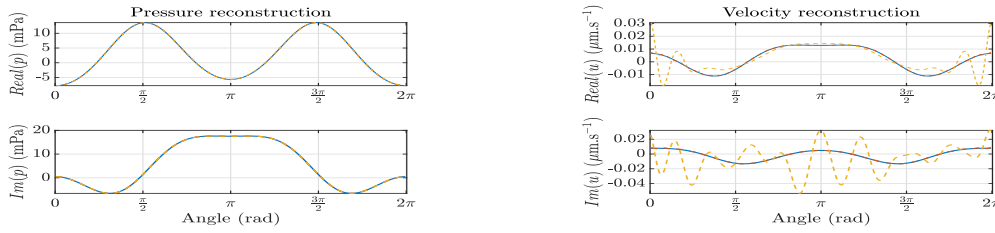


Figure 4: Pressure (left) and velocity (right) reconstructions at 3 kHz in the "noisy" (yellow dashed curve) and "noiseless" (red dashed curve) configurations, together with the reference fields (blue continuous curve) obtained with the sound scattering model from section 2.

#### 4.4. Impedance estimation results

Figure 5 shows the impedance estimation error relatively to the impedance model shown Figure 2. In the "noiseless" configuration, the error does not exceed 4% on the whole frequency range and decreases with frequency.

In the "noisy" case, the error is about 100 % from 1 to 7 kHz. Remind that below 7 kHz, the impedance of the cylinder's coating was higher than  $1000 \rho_0 c_0$  in absolute value. These high impedance values make the velocity reconstruction challenging, as explained earlier. Above 7 kHz, the impedance estimation error becomes lower than 50% and decreases with frequency, which shows that the impedance estimate is consistent.

## 5 Preliminary experiment

An estimate of the impedance of the skin of a human arm is experimentally obtained with the impedance estimation method proposed in this work. The results of this experiment are introduced in this section.

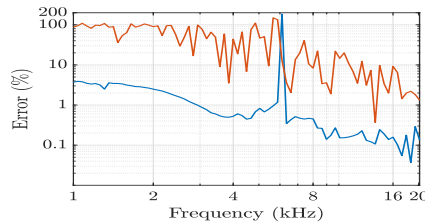
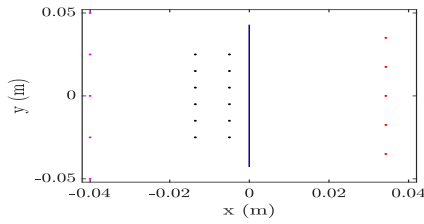


Figure 5: Impedance estimation error relatively to the impedance model shown on Figure 2. Results shown for the "noiseless" (blue curve) and "noisy" (red curve) configuration.

The measurements for this experiment are performed in the small anechoic chamber of the Acoustic Department of the Technical University of Denmark. Sound pressure measurements are performed on a line close to a human forearm, as depicted Figure 6a. The test subject was a male of age 25, measuring around 180 cm and of body weight 65 kg. He was asked to firmly place his arm on a support and to present his inner forearm to a microphone as shown Figure 6b. A Universal Robots UR5 robotic arm is used to scan the measurement points with high precision. An 1/8 inch microphone is attached to a rigid rod connected to the robotic arm in order to avoid scattering from the arm. The setup used for the ESM reconstruction is shown Figure 6a. A two dimensional measurement geometry is chosen.

Pressure averaging on 16 realizations and sixth octave frequency bands are performed as the impedance estimation method is expected to be very sensitive to noise as seen in the numerical tests in section 4. The reconstruction is made on the forearm surface, which is roughly plane and is shown as a blue line Figure 6a. The normal impedance of skin is then estimated as the mean on the whole reconstruction surface.

The estimated impedance of the skin of the subject's forearm is shown Figure 7a on the frequency range [10.3,13] kHz. A preliminary study of the experimental conditions showed that the frequency response of the



(a)



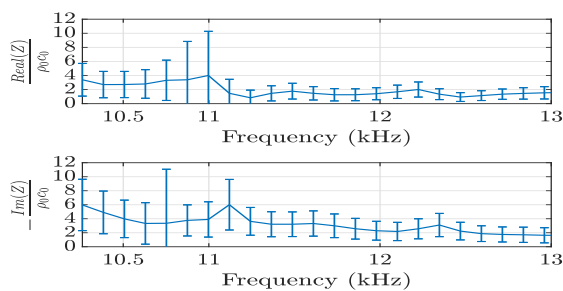
(b)

Figure 6: Left : Setup used for the experimental test of the ESM reconstruction. Blue line: reconstruction surface, red dots: inner equivalent sources, magenta dots: outer equivalent sources, black dots: measurement points. 6 measurement points are located 5 mm away from the arm's surface, and 6 other are located 13.5mm away from it. There are 5 inner equivalent sources retracted 34.3 mm away from the surface of the arm, and 5 outer equivalent sources 40 mm away from the surface. Right : Photograph of the experimental setup.

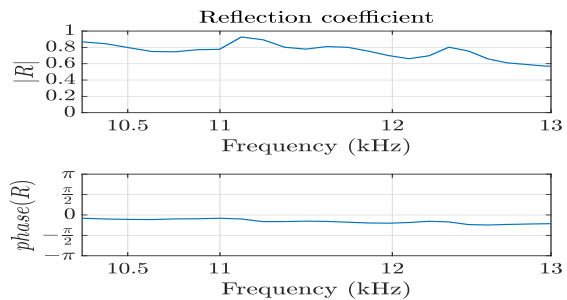
speaker used in the experiment presented a broad notch centered on 17 kHz. This was due to scattering from the edges of the speaker, and led to a poor signal to noise ratio from 14 to 20 kHz.

On Figure 7a, the reactive part of the estimated impedance is higher than its resistive part in absolute value. It is also negative and its amplitude is decreasing inversely proportional to frequency, which is characteristic of a compliant behaviour. This behaviour is consistent with the one that resulted from the scattering model developed in section 2. The order of magnitude of the estimated impedance is significantly lower than the one obtained with the scattering model which involved a silicone layer on a rigid body, although it seems to correspond to the orders of magnitude measured in [5]. Indeed, a thin silicone layer backed by a rigid baffle is considerably harder than human skin.

The reflection coefficient corresponding to the estimated impedance is shown Figure 7b. It is about 0.8 from 10.3 to 11.8 kHz, and it decreases to 0.6 between 11.8 and 13 kHz.



(a)



(b)

Figure 7: Left : Estimated impedance of the skin of the subject's forearm in the experimental attempt, together with the standard deviation of the impedance on the reconstruction surface. Right: Amplitude (top) and phase (bottom) of the reflection coefficient of skin inferred from the impedance estimate shown on the left figure.

## 6 Discussion

The theoretical model derived in section 2 and numerically constructed in section 4 leads to consistent results but still needs to be validated, e.g. with a numerical model based on the finite element method. Using the mechanical properties of silicone, the cylinder's normal impedance has been shown to be significantly higher in absolute value than the one experimentally obtained in [5] for human skin. Later on, choosing a material softer than silicone could improve the proposed model of sound scattering by a human arm.

The numerical tests of the proposed method on the scattering model in section 4 show that the impedance

estimation method behaves well in absence of noise. However, the sensitivity to noise of the method is highlighted by the tests, which shows the need to improve the method. Using velocity measurements would for example allow to get rid of the noise amplification in the velocity reconstruction.

In section 5, the estimate of the impedance of the skin of a subject's forearm presents the compliant behaviour that was observed in the results of the scattering model. Moreover, the orders of magnitude of the estimated impedance correspond to the ones measured by [5]. The resulting reflection coefficient is lower than the ones obtained for skin in [5] and [20], which calls for an experimental validation of the method with an object of known impedance, a measurement campaign on a broader sample of subjects, and improvements of the experimental setup.

The ESM reconstruction on the surface of the forearm leads to inconsistent results under 10 kHz. This could be due to the use of a two dimensional ESM setup, which implies an infinite extent of the forearm. The forearm of the test subject measuring about  $l = 20$  cm, the frequency above which the forearm would measure 6 times more than the acoustic wavelengths would be  $f_{min} = 6 \frac{c_0}{l} \approx 10.3$  kHz. This frequency coincides to the lower bound of the frequency range where the estimated impedance was consistent.

An attempt of experimental validation of the method on a silicone cylinder such as the one studied in section 2 was also performed. It is not included in this work as it resulted in inconsistent results. However, it highlighted some practical challenges that will have to be overcome. Acoustic scattering from the objects used in the measurement setup (support used for the object of interest, robotic arm) and vibrations of the support of the object under study were identified as two significant sources of discrepancies.

## 7 Conclusion

This study has examined a methodology for estimating the impedance of non-porous elastic materials. In section 2, a theoretical solution to the problem of scattering of sound by an elastic cylinder was derived. The solution was built numerically in section 4. It led to consistent results in terms of acoustic pressure when compared to the solution obtained for a rigid cylinder. The frequency behaviour of the silicone layer's impedance was close to the one inferred from measurements on skin in [5]. However, the high values of impedance obtained with the model show the need for a material softer than silicone to emulate skin.

In section 4, the ESM was applied to the solution of the scattering problem. The pressure at the surface of the scattering cylinder was reconstructed successfully, while the velocity reconstruction was shown to be sensitive to noise due to the high impedance of the cylinder on the lower end of the frequency range of interest. The impedance estimation based on the ESM reconstruction was biased by this source of error. However, at higher frequencies, the cylinder's impedance was lower which led to a more consistent impedance estimate. Further work will be necessary to improve the velocity reconstruction.

In section 5, a first attempt of estimation of the impedance of human skin was performed. This preliminary experiment suffered from a few sources of significant errors. However, a compliant behaviour was observed on a limited frequency range and the order of magnitude were consistent with the ones obtained in [5]. This motivates further studies on the use of near field acoustic holography to estimate the impedance of skin or other elastic materials.

## Acknowledgements

The authors would like to express their gratitude to the Danish Acoustic Society (DAS-fonden), which granted the participation to the conference.

## References

- [1] Christopher J. Plack. *The sense of hearing*. Routledge, Abingdon, Oxon ; New York, NY, third edition, 2018.

- [2] Sechler et al. Virtual reality sound localization testing in cochlear implant users. In *2017 8th International IEEE/EMBS Conference on Neural Engineering (NER)*.
- [3] Nishino et al. Interpolating HRTF for auditory virtual reality. *The Journal of the Acoustical Society of America*, 100:2602–2602, 1996.
- [4] Nouredine Atalla and Franck Sgard. *Finite element and boundary methods in structural acoustics and vibration*. CRC Press, Boca Raton, 2015. OCLC: ocn911263399.
- [5] Théo Auclair. Influence of surface impedance on the sound field around a head and torso simulator. Master's thesis, Technical University of Denmark, Acoustic Technology, 2019.
- [6] Hald et al. In-situ impedance and absorption coefficient measurements using a double-layer microphone array. *Applied Acoustics*, 143:74, 08 2018.
- [7] Mélanie Nolan. Estimation of angle-dependent absorption coefficients from spatially distributed in situ measurements. *The Journal of the Acoustical Society of America*, 147:EL119–EL124, 02 2020.
- [8] Antoine Richard. *Characterization of acoustic properties of surfaces based on spatio-temporal information*. PhD thesis, Technical University of Denmark, Acoustic Technology, 2018.
- [9] Gary H. Koopmann, Limin Song, and John B. Fahnlne. A method for computing acoustic fields based on the principle of wave superposition. *The Journal of the Acoustical Society of America*, 86(6):2433–2438, December 1989.
- [10] Simone Sternini et al. Bistatic scattering of an elastic object using the structural admittance and noise-based holographic measurements. *The Journal of the Acoustical Society of America*, 148(2):734–747, August 2020.
- [11] Efren Fernandez-Grande, Finn Jacobsen, and Quentin Leclère. Sound field separation with sound pressure and particle velocity measurements. *The Journal of the Acoustical Society of America*, 132(6):3818–3825, December 2012.
- [12] Nicolas P. Valdivia and Earl G. Williams. Study of the comparison of the methods of equivalent sources and boundary element methods for near-field acoustic holography. *The Journal of the Acoustical Society of America*, 120(6):3694–3705, December 2006.
- [13] Lin JH. Bai MR, Chen CC. On optimal retreat distance for the equivalent source method-based nearfield acoustical holography. *Journal of The Acoustical Society of America - JACOUST SOC AMER*, 129:1407–1416, 03 2011.
- [14] Angie Sarkissian. Method of superposition applied to patch near-field acoustic holography. *Journal of The Acoustical Society of America - JACOUST SOC AMER*, 118:671–678, 08 2005.
- [15] Finn Jacobsen and Peter Moller Juhl. *Fundamentals of general linear acoustics*. John Wiley & Sons Inc, Chichester, West Sussex, United Kingdom, 2013.
- [16] James J. Faran. Sound Scattering by Solid Cylinders and Spheres. *The Journal of the Acoustical Society of America*, 23(4):405–418, July 1951.
- [17] J. Gomes. A study on regularization parameter choice in Near-field Acoustical Holography. In *2008 7th European Conference on Noise Control (EURONOISE)*, pages 2875–2880, 2008. ISSN: 2226-5147.
- [18] Tieneng Guo, Yunchao Gu, Shiming Ma, and Li Wang. Dynamic mechanical properties of ZN-35 silicone rubber materials based on H-N model. In *2016 4th International Conference on Machinery, Materials and Computing Technology*, January 2016.
- [19] Todd M. Mower. Thermomechanical behavior of aerospace-grade RTV (silicone adhesive). *International Journal of Adhesion and Adhesives*, 87:64–72, December 2018.
- [20] Brian F. G. Katz. Acoustic absorption measurement of human hair and skin within the audible frequency range. *The Journal of the Acoustical Society of America*, 108(5):2238–2242, November 2000.